

Non-linear aero-elastic response of a multi-layer TPS

P. Pasolini^{*1}, E. H. Dowell², S. De Rosa¹, F. Franco¹ and R. Savino¹

¹Department of Industrial Engineering (DII), University of Naples "Federico II", Italy

²Department of Mechanical Engineering and Materials Science, Duke University, U.S.A.

(Received December 2, 2016, Revised December 5, 2016, Accepted December 6, 2016)

Abstract. The aim of the present work is to present a computational study of the non-linear aero-elastic behavior of a multi-layered Thermal Protection System (TPS). The severity of atmospheric re-entry conditions is due to the combination of high temperatures, high pressures and high velocities, and thus the aero-elastic behavior of flexible structures can be difficult to assess. In order to validate the specific computational model and the overall strategy for structural and aerodynamics analyses of flexible structures, the simplified TPS sample tested in the 8' High Temperature Tunnel (HTT) at NASA LaRC has been selected as a baseline for the validation of the present work. The von Kármán's three dimensional large deflection theory for the structure and a hybrid Raleigh-Ritz-Galerkin approach, combined with the first order Piston Theory to describe the aerodynamic flow, have been used to derive the equations of motion. The paper shows that a good description of the physical behavior of the fabric is possible with the proposed approach. The model is further applied to investigate structural and aero-elastic influence of the number of the layers and the stitching pattern.

Keywords: aero-elasticity; atmospheric re-entry; non-linearity

1. Introduction

Even though the subsonic and supersonic aero-elastic stability of plates has been studied starting from the late 1960s (Dugundji 1966, Dowell 1975), it is still a subject of current investigations. While some work has been done on panel aero-elastic and aero-thermo-elastic behavior (Mei *et al.* 1999, Dowell 1970), there are only a handful of papers that specifically address membrane flutter (Ellen 1965). Even if the term membrane is reserved for zero bending rigidity structures, almost all of these studies consider the membrane flutter problem to be a limiting case of a plate as bending rigidity approaches zero, or in-plane tension approaches infinity (Spriggs *et al.* 1969, Johns 1971, Scott *et al.* 2007).

Currently the state-of-art of the Computational Aero Thermo Elasticity (CATE) study is the closely coupled model, wherein the fluid and structure equations are solved separately using different solvers, but are coupled into one single module with exchange of information at the interface using an interface module thereby making the entire model tightly coupled.

Fig. 1 shows the fluid and structure solvers along with the methodologies for aero-elastic

*Corresponding author, Ph.D., E-mail: pietro.pasolini@unina.it

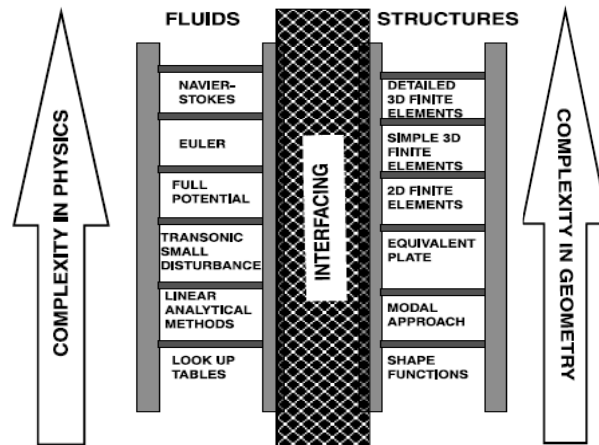


Fig. 1 Fluid and structure solvers for aero-elastic simulation for a closely coupled model (Guruswamy 2002)

simulation for a closely coupled model (Guruswamy 2002).

Due to the challenging hypersonic flow regime and the complexity of coupling fluid and structural solvers in an accurate and computationally efficient manner, high-fidelity computational modeling of flexible inflatable TPS has been limited (Rohrschneider 2007, Wang *et al.* 2010, Kramer *et al.* 2013).

On the one hand, the aero-thermo-elastic analysis using coupled CFD-FEM approaches provides accurate results; on the other hand, it presents a significant computational cost due to very large numbers of degrees of freedom. It is for that reason that we need to provide theoretical and experimental non-linear tools capable of give us a preliminary indication of the aero-thermo-elastic behavior of the structure.

In order to overtake the computational cost problem related to the fluid-structure-interaction coupling, Goldman and Dowell have studied the possibility of coupling a simplified nonlinear structural theory based on a hybrid Ryleigh-Ritz-Galerkin method (Goldman and Dowell 2014) with the first-order Piston Theory (PT) aerodynamics (Goldman *et al.* 2013, Goldman *et al.* 2014, Goldman *et al.* 2015). Several studies (McNamara and Friedmann 2007) have proven that the accuracy of the PT diminishes with increasing Mach number and surface inclination to the free stream. However computational efficiency and ease of implementation still make this method attractive for preliminary design of hypersonic configurations. A good approximate criterion for the accuracy of PT is that the product of Mach number and surface inclination is less than one (McNamara and Friedmann 2007). Due to the recent interest in new and innovative structural concepts for the space exploration, especially those related to the flexible TPSs on inflatable and deployable aerodynamic decelerators, the investigation of the subsonic and supersonic aero-elastic stability of membranes has received a new thrust. Several studies on the development of a deployable TPS have been carried out by Savino *et al.* (2012), (2013) and Carandente *et al.* (2014).

Furthermore, NASA and several academic researchers have carried out several works on the Hypersonic Inflatable Aerodynamic Decelerator (HIAD) technology (Wilde and Walther 2001). The most advanced program, including experimental flight test and aero-elastic assessments, is the Inflatable Re-entry Vehicle Experiment (IRVE) (Hughes *et al.* 2005, Dillman *et al.* 2010, Dillman

et al. 2013).

The characteristics that make this configuration so attractive is the possibility to accommodate the heat shield in a folded configuration at launch, and then to be deployed only during the entry phase, offering the advantage to increase the mass/volume ratio at launch, and widening the choice of available launchers. Furthermore, when deployed, the ballistic coefficient is relatively low, implying a large deceleration in the upper rarefied region of the atmosphere, with consequent reduction of the thermal and dynamic loads.

The purpose of this work is to present an analysis of the influence of the number of layers and the stitching pattern on the aero-elastic behavior of a simply supported square Thermal Protection System (TPS), using a theoretical approach based on the modes extraction and the von Kármán's three-dimensional large deflection theory. The theory behind the present work has been preliminarily investigated by Goldman and Dowell (Goldman *et al.* 2014).

The paper is organized as follows. In Section 2, the modal-based (MB) non-linear computational method has been presented. The experimental model, at the basis of the numerical validation of this work, has been presented in Section 3. Such method has been validated in Section 4. Finally, the non-linear aero-elastic main results and conclusions are summarized in Sections 5 and 6.

2. Computational method

In order to evaluate the dynamic behavior of the specimen, the von Kármán's three dimensional large deflection theory (Dowell 1975) and an hybrid Raleigh-Ritz-Galerkin approach (Goldman *et al.* 2014) have been used to derive the equations of motion. Using this approach, we need to describe the Lagrangian of the problem.

$$L = T - U \quad (1)$$

Where T is the kinetic energy

$$T = \int_0^a \int_0^b \frac{m}{2} \left(\frac{\partial w}{\partial t} \right)^2 dx dy \quad (2)$$

and U is the elastic potential energy

$$U = U_B + U_S + U^{St} \quad (3)$$

U_B and U_S represent the bending and stretching energies given by von Kármán's large deflection theory for a single plate layer respectively (see Eq. (4)). The principal source of structural non-linearity is the tension that results from the in-plane stretching energy U_S that is a consequence of the large out-of-plane bending.

$$U_B = \frac{D}{2} \int_0^b \int_0^a \left\{ \left(\frac{\partial^2 w}{\partial x^2} \right)^2 + \left(\frac{\partial^2 w}{\partial y^2} \right)^2 + 2\nu \frac{\partial^2 w}{\partial x^2} \frac{\partial^2 w}{\partial y^2} + 2(1-\nu) \left(\frac{\partial^2 w}{\partial x \partial y} \right)^2 \right\} dx dy \\ + \frac{N_x^A}{2} \int_0^b \int_0^a \left(\frac{\partial w}{\partial x} \right)^2 dx dy + \frac{N_y^A}{2} \int_0^b \int_0^a \left(\frac{\partial w}{\partial y} \right)^2 dx dy \quad (4)$$

$$U_S = \frac{1}{2Eh} \int_0^b \int_0^a \left\{ \left(\frac{\partial^2 F}{\partial x^2} \right)^2 + \left(\frac{\partial^2 F}{\partial y^2} \right)^2 + 2\nu \frac{\partial^2 F}{\partial x^2} \frac{\partial^2 F}{\partial y^2} + 2(1-\nu) \left(\frac{\partial^2 F}{\partial x \partial y} \right)^2 \right\} dx dy$$

Where F is the Airy stress function for a given layer. An expression of the Airy stress function is given below.

$$\left(\frac{\partial^2 F}{\partial x^2}\right) = N_y ; \left(\frac{\partial^2 F}{\partial y^2}\right) = N_x ; \left(\frac{\partial^2 F}{\partial x \partial y}\right) = N_{xy} \quad (5)$$

For point-wise tack locations, the stitching energy (U^{St}) may be written as shown in Eq. (6). In this formulation, we assume the stitches constraining the several layers are represented by simple linear springs with k^{St} equal to the spring constant of the stitch. The stitching energy may take different forms depending on the desired pattern. Eq. (6) shows the stitching energy where the first term represents the point-wise stitching between the first and the second layers, and the second term represents the point-wise stitching between the second and the third layers. The summation indices indicate the number of stitches.

$$U^{St} = \frac{k^{St}}{2} \sum_i (w^{L1} - w^{L2})^2 |_{x_i, y_i} + \frac{k^{St}}{2} \sum_i (w^{L2} - w^{L3})^2 |_{x_i, y_i} \quad (6)$$

In order to assess the aero-elastic behavior of the TPS the first order Piston Theory (PT) (Dowell 1975) will be used. An expression of the aerodynamic virtual work is given by Eq. (7).

$$\delta W_{aero} = - \int_0^b \int_0^a (\Delta p \delta w) dx dy \quad (7)$$

Where the aerodynamic pressure (Δp) is given by first-order PT

$$\Delta p = \frac{2q}{Mach} \left[\frac{\partial w}{\partial x} + \frac{1}{V_\infty} \frac{\partial w}{\partial t} \right] \quad (8)$$

Furthermore, in order to satisfy simply supported deflection boundary conditions as well as a condition of vanishing axial stress the deflection and Airy stress function are expanded in modal form using the modeshape function $\phi_{nm}(x, y)$

$$\phi_{nm}(x, y) = \sin\left(\frac{n\pi x}{a}\right) \sin\left(\frac{m\pi y}{b}\right) \quad (9)$$

$$w = \sum_n \sum_m q_{nm}(t) \phi_{nm}(x, y) ; F = \sum_n \sum_m f_{nm}(t) \phi_{nm}(x, y) \quad (10)$$

The stress function expansion is an approximate particular solution to the following strain compatibility condition (Dowell 1975).

$$\frac{\nabla^4 F}{Eh} = \left(\frac{\partial^2 w}{\partial x \partial y}\right) - \frac{\partial^2 w}{\partial x^2} \frac{\partial^2 w}{\partial y^2} \quad (11)$$

A Galerkin approach is used to solve equation 11 for the stress function modal coordinate f_{nm} , in terms of the deflection coordinate q_{nm} .

The Lagrangian is then written in terms of deflection coordinates only, and the Lagrange equation of the following form is applied

$$\frac{d}{dt} \left(\frac{\partial L}{\partial \dot{q}_{nm}} \right) - \frac{\partial L}{\partial q_{nm}} + Q_{nm} \quad (12)$$

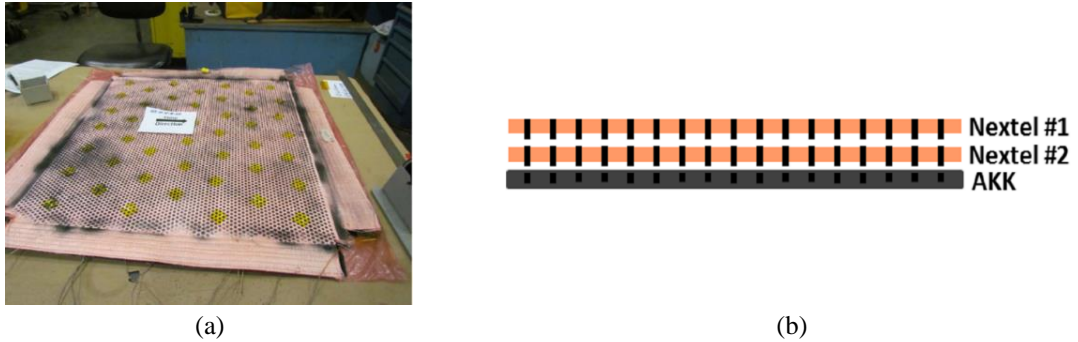


Fig. 2 TPS sample layout (Goldman *et al.* 2014)

Table 1 Material properties of the TPS layers

Material	Young's modulus E (GPa)	Poisson's ratio ν	Mass/area (Kg/m ²)	Thickness (mm)
Nextel 440-BF20	190	0.26	0.46	0.508
Aluminized Kapton Kevlar (AKK)	124	0.36	0.14	0.154

Where Q_{nm} is the generalized force.

Substituting $w (q_{nm}(t), \phi_{nm}(x, y))$ into the energy equations and rewriting the Lagrange equation in a matrix form, we obtain a system of non-linear integro-differential equations, which for the three-layer case assume the formulation that follows (see Eq. (13))

$$\begin{aligned}
 M^{N1} \ddot{\vec{a}} + Z^{N1} \dot{\vec{a}} + D^{N1} \vec{a} + [B^{N1} + A^{N1}] \vec{a} + I^{N1} \{ \vec{a} - \vec{b} \} + S^{N1} &= 0 \\
 M^{N2} \ddot{\vec{b}} + D^{N2} \dot{\vec{b}} + B^{N2} \vec{b} + I^{N2} \{ \vec{b} - \vec{c} \} + I^{N2} \{ \vec{b} - \vec{a} \} + S^{N2} &= 0 \\
 M^K \ddot{\vec{c}} + D^K \dot{\vec{c}} + B^K \vec{c} + I^K \{ \vec{c} - \vec{b} \} + S^K &= 0
 \end{aligned}
 \tag{13}$$

Where \vec{a} , \vec{b} and \vec{c} are the modal coordinate vectors of the three layers M^{layer} , B^{layer} , D^{layer} , I^{layer} and S^{layer} are the diagonal mass matrix, the diagonal bending stiffness matrix, the diagonal damping matrix, the spring stitching matrix and the stretching energy vector respectively. Therefore, since the principal source of structural non-linearity is the tension that results from the in-plane stretching, the non-linearity of the system lies in the stretching energy vector S^{layer} . Furthermore, Z^{layer} and A^{layer} are the aerodynamic damping and the aerodynamic stiffness matrix respectively. The superscript N1, N2 and K indicate the first and the second layer of the Nextel, and the third Kapton layer respectively. An extended formulation of the aforementioned matrices has been reported in the work done by Goldman and Dowell (2014).

Furthermore, in addition to the aero-elastic analysis, an impulse analysis has been performed. This calculation has been developed in order to experimentally validate the procedure presented with GVTs performed on the test article used by Goldman (2014). For the impulse analysis, the aerodynamic stiffness and damping terms for the outermost Nextel layer are removed and replaced with the external force vector F^e (see Eq. (14)).

$$F^e = F_{app} \delta(t - t_0) \phi(x, y) \Big|_{x_0, y_0}
 \tag{14}$$

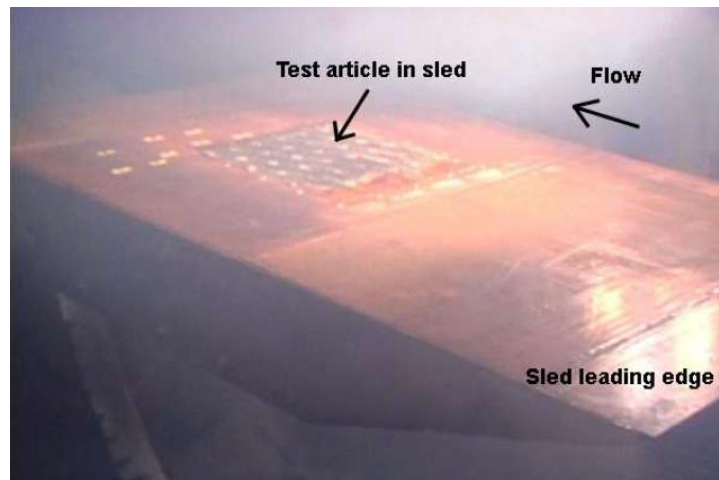


Fig. 3 TPS sample mounted in the 8' HTT sled at 5° angle of attack (Goldman *et al.* 2014)

Table 2 Measured mach number and dynamic pressure in the 8' HTT (Goldman *et al.* 2014)

Angle of Attack (AoA)	Local Mach Number	Dynamic Pressure (Pa)
0	5.8	33094
2.5	5.6	46884
5	5.35	60763
7.5	5.1	74463
10	4.8	88252

Finally, in order to assess the aero-elastic behavior of the TPS the Eq. (13) is solved using the 4th order Runge-Kutta integration scheme in MATLAB.

3. The test article

The TPS specimen chosen as reference for this study is a square TPS tested in the 8' High Temperature Tunnel (HTT) (see Fig. 2). The size of the sample is 60 cm×60 cm and it is the same sample used by Goldman *et al.* (2014).

The test article consists of two layers of Nextel 440-BF20 and one layer of Aluminized Kapton Kevlar (AKK), stitched together in a 5 cm square pattern.

Material properties of the Nextel and the AKK are given in Table 1.

Before to test the square TPS sample in the 8'HTT, Ground Vibration Tests (GVTs) using two accelerometers and a transducer hammer have been performed. Those tests have been carried out with and without tension, in and out of the tunnel sled, and pre-and post-tunnel run.

Fig. 3 shows the TPS sample mounted in the 8'HTT facility at NASA LaRC in Virginia.

Table 2 shows Mach numbers and dynamic pressures experienced by the sample test in the 8' HTT as a function of the Angle of Attack (AoA). The tunnel run time is also limited to a maximum of 90 seconds, since the compressed air and liquid oxygen needed for a single run are stored in a bottle farm with a fixed capacity.

Table 3 Natural frequencies of the TPS sample

Mode	Natural frequencies (Hz)				
	Untensioned	Tensioned (525 N/m)	Mode	Untensioned	Tensioned (525 N/m)
1,1	17.97	48.85	3,3	161.66	211.50
1,2 - 2,1	44.92	84.71	3,4 - 4,3	224.42	276.15
1,3 - 3,1	89.85	135.60	3,5 - 5,3	304.95	358.30
1,4 - 4,1	152.69	202.18	3,6 - 6,3	403.02	457.87
1,5 - 5,1	233.38	285.32	4,4	287.08	340.10
1,6 - 6,1	331.74	385.53	4,5 - 5,4	367.41	421.74
2,2	71.88	115.84	4,6 - 6,4	465.17	520.88
2,3 - 3,2	116.79	164.49	5,5	447.43	502.90
2,4 - 4,2	179.60	230.08	5,6 - 6,5	544.68	601.51
2,5 - 5,2	260.24	312.76	6,6	641.13	699.43
2,6 - 6,2	358.50	412.70			

4. Model validation

In order to validate the computational model summarized in Section 2, a comparison between an impulse analysis and the GVTs results, and between a numerical aero-elastic analysis and tunnel tests results on the 3 layered TPS model presented in Section 3 have been made.

Before evaluating the non-linear aero-elastic response of the fabric, it is of interest to calculate the linear natural frequencies of the TPS first, neglecting the non-linear term S^{layer} of the Eq. (13). Since it is preferred to have all three layers connected together to prevent hot gas from damaging the body of the entry capsule, a stitching stiffness k^{St} of 50000 (Nm) has been chosen for the computational model.

Since we are expecting the lower modes and natural frequencies are most important for the flutter behavior of the TPS, a total of 36 half-waves (6 on the x direction and 6 on the y direction) has been selected for the linear analysis. A comparison among natural frequencies of the three-layer fabric, including a pre-tension of 525 N/m as applied to the experimental specimen, using eigenvalue extraction, has been summarized in Table 3.

Then, in order to compare non-linear analytical results with GVTs results, a dynamic response to an impulse force has been numerically developed. Values of 0.01 and 0.001(N) have been set for the critical structural damping and the impulse force amplitude (F_{app}) respectively. In order to excite the greatest number of modes in the frequency interval of our interest, the force has been applied in a point with $x_0, y_0=0.1$. As done for the linear case, a number of 36 half-waves (6 on the x direction and 6 on the y direction) has been selected for the non-linear analysis.

The Fast Fourier Transform (FFT) of the structural responses is not a fully correct approach to compare the results with the linear natural frequency computation due to the non-linear characteristics of the present problem. Nevertheless, it allows one to verify the matching of peak frequencies and a first assessment of the overall structural response. For the above-mentioned reasons and due to some uncertainties about the experimental measurements, the successive plots report only normalized results. Fig. 4 shows the comparison between the experimental GVTs and the numerical FFT results normalized by the maximum FFT amplitude for the untensioned (a) and the pre-tensioned (b) case.

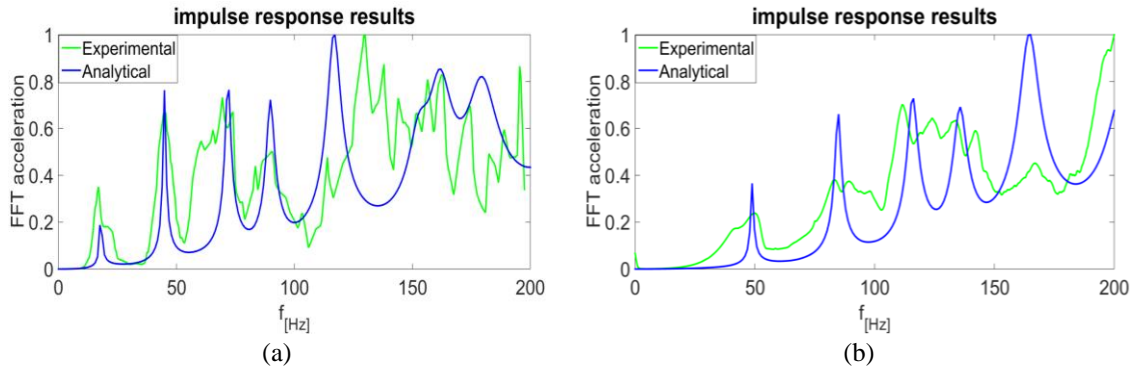


Fig. 4 Non-linear impulse response comparison: (a) Untensioned, and (b) pre-tensioned

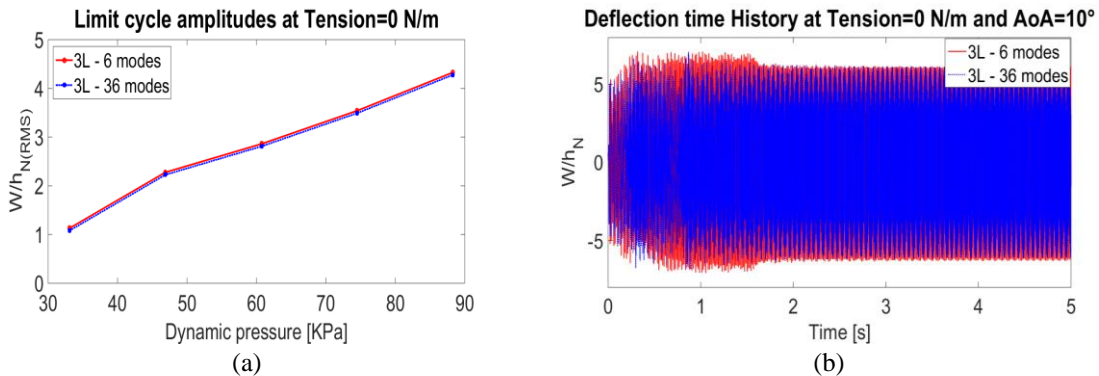


Fig. 5 (a) Limit cycle amplitudes as a function of dynamic pressure untensioned and (b) deflection time history at x/a , $x/b=0.8, 0.5$, $AoA=10^\circ$, untensioned

In the aero-elastic experiment carried out at NASA LaRC two tunnel tests have been conducted for the case with the three-layer TPS sample, labelled as #RUN22 and #RUN23, respectively. The difference between the two runs is how the angle of attack was changed in time. For the #RUN22, the tunnel was initially set at 5° for 5 seconds and 2.5° for 3 seconds. For #RUN23, the tunnel was initially set at 2.5° for 3 seconds and 5° for 5 seconds. This procedure was implemented to see if the response trends were path dependent.

Since it is expected that the influence of the modes with the half-waves in the flow direction is greatest, and in order to reduce the computational time, 6 half-waves in the flow direction and 1 half-wave in the spanwise direction have been selected. In order to prove the validity of this assumption, an aero-elastic calculation taking into account 36 modes (6 span-wise and 6 stream-wise) has also been carried out, for the untensioned case. Deflection time histories at the accelerometer location near the trailing edge of the sample, located at x/a , $y/b=0.8, 0.5$, as a function of flow Mach number and dynamic pressure summarized in Table 2 were computed using the non-linear numerical procedure previously outlined. Because of the solution is chaotic in time the Root Mean Square (RMS) amplitude has been used as a measure of deflection magnitude. Since the objective of this simulation is to check the convergence of the solution, the simulation time has been set to 5 seconds. Fig. 5 shows that there is no difference in terms of w/h_N (RMS) amplitudes between the simulation with 36 modes and the simulation with only 6 modes (a), and a

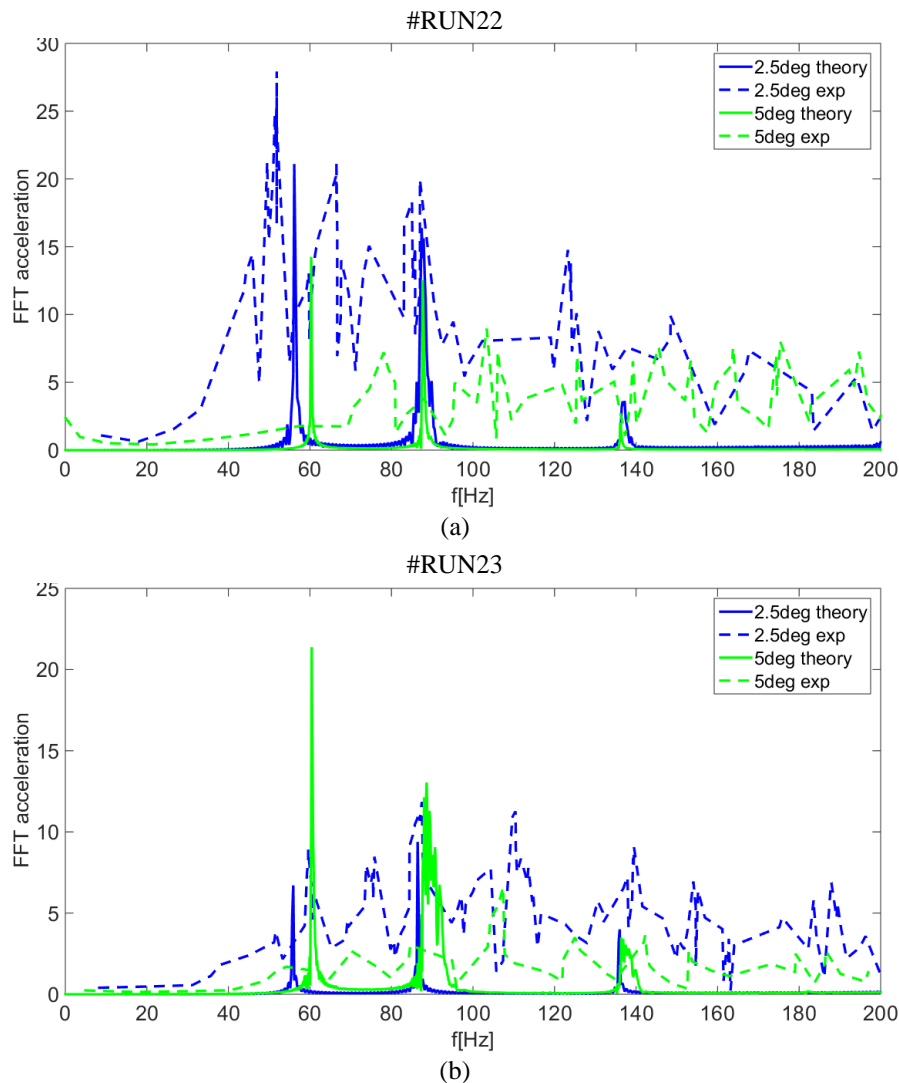


Fig. 6 Non-linear response comparison between experiment and theory for #RUN22 (a) and #RUN23 (b) at $x/a, x/b=0.8,0.5$

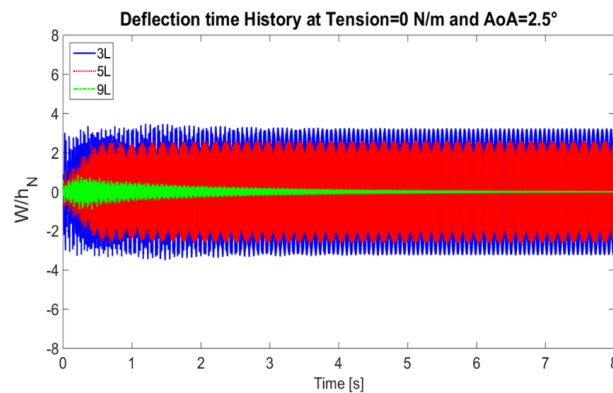
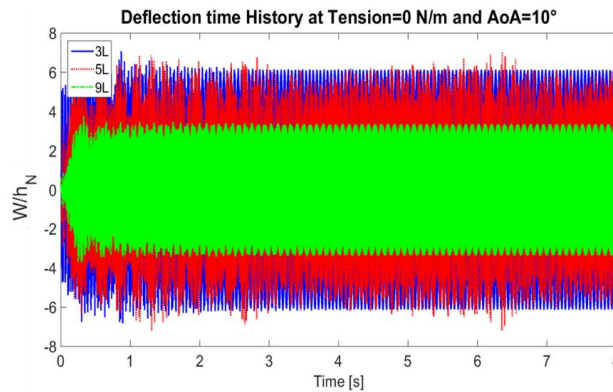
comparison of the deflection time histories for the critical case at an AoA of 10° has been shown (b).

Theoretical and experimental FFTs of the deflection time histories for the TPS sample and tunnel #RUN22 and #RUN23, are measured at the accelerometer location.

Fig. 6 shows the results for the theoretical and experimental frequency spectra. The theoretical model reasonably predicts the peak frequency and amplitude for both runs. The small uncertainty of the results may be due to excitation sources neglected in the present computational model such as turbulent boundary layer fluctuations inside the wind tunnel, the initial condition chosen, and/or the structural damping. Despite these sources of uncertainty, the present result shows good agreement in terms of peak frequency and amplitude between theory and the experiment.

Table 4 Natural frequencies comparison

Frequency	3L (Hz)		5L (Hz)		9L (Hz)	
	Untensioned	Pre-tensioned	Untensioned	Pre-tensioned	Untensioned	Pre-tensioned
f_{11}	17.97	48.85	18.55	46.75	18.86	45.54
f_{21}	44.93	84.71	45.37	82.18	47.16	80.73
f_{31}	89.85	135.61	92.75	133.45	94.31	132.23
f_{41}	152.7	202.18	157.62	201.29	160.3	200.79
f_{51}	233.38	285.32	240.94	286.52	245.04	287.19
f_{61}	331.74	385.53	342.53	389.58	348.36	391.8

Fig. 7 Deflection time history comparison at $x/a, x/b=0.8,0.5$, $AoA=2.5^\circ$, untensionedFig. 8 Deflection time history comparison at $x/a, x/b=0.8,0.5$, $AoA=10^\circ$, untensioned

5. Results and analysis

5.1 The influence of the number of layers on the aero-elastic response

For both structural and thermal considerations, it may be required to increase the number of layers of the TPS. In this section the aero-elastic behavior of three different situations, with different layer configurations, is investigated.

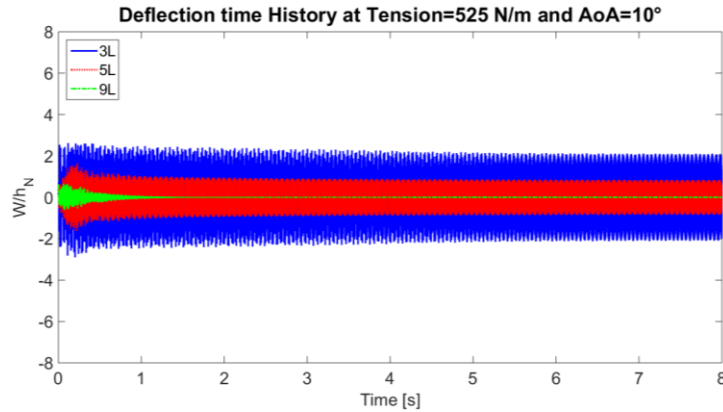


Fig. 9 Deflection time history comparison at $x/a, x/b=0.8,0.5$, $AoA=10^\circ$, pre-tensioned

Before calculating the aero-elastic response, it is of interest to calculate the natural frequencies of the TPS using linear theory. As before, the plate nonlinearities are ignored for this purpose, neglecting the S^{layer} term of the Eq. (13).

Three Test Cases (TCs) have been investigated: the three-layer (3L), the five-layer (5L) and the nine-layer (9L). For all the test cases, only the last layer is made of AKK, while the other layers are made of Nextel 440 BF-20; all of the layers are stitched together in a 5 cm square pattern. This choice has been made in order to simulate a real case, in which it is important to limit heating on the backside of the sample and gas penetration during a test, or the atmospheric entry. As chosen for the validation of the 3L model, 6 half-waves on the flow field direction and 1 half-wave on the span wise direction has been selected for the computational model. A pretension of 525 N/m has also been set for each TC. The critical structural damping has been set to 0.01 and a stitching stiffness k^{St} of 50000 (Nm) has been chosen.

Natural frequencies for each TC have been summarized in Table 4.

As expected, increasing the number of layers for the untensioned case increases the natural frequency of each mode. Otherwise, by pre-tensioning the TPS, because of the increase of the thickness of the whole TPS, the natural frequencies of the first four modes tend to decrease but after the 4th mode, the natural frequency increases.

Deflections time histories, at the accelerometer location, as a function of flow Mach number and dynamic pressure (summarized in Table 2), were computed using the non-linear computational model outlined in section 2. The simulation time (8 sec) has been set to enable an investigation of the steady state.

Fig. 7 shows the deflection time history of the three different TCs in a particular condition, when the AoA is equal to 2.5° for the untensioned case. As shown, the deflections of the TCs 3 L and 5 L, after a short transient experience a non-linear vibrational phenomenon known as the Limit Cycle Oscillation (LCO). However the response of the TC 9L decays with the time. Furthermore, Fig. 8 shows the deflection time history of the three different TCs when the AoA is equal to 10° . As shown in this case, all three TCs are experience LCO, with amplitudes higher than the case at 2.5° .

Fig. 9 shows the deflection time history of the three TCs, at the accelerometer location, at the AoA equal to 10° for the pre-tensioned case. As shown, while the deflection amplitude of the TC 9L decays after a short transient, the deflection amplitudes of the TCs 3 L and 5 L seem to reach a

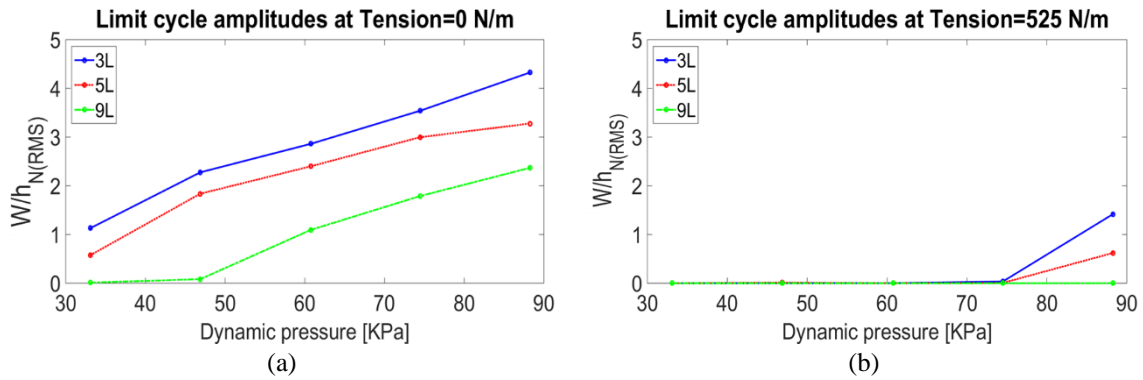


Fig. 10 Limit cycle amplitudes as a function of dynamic pressure untensioned (a) and tensioned (b)

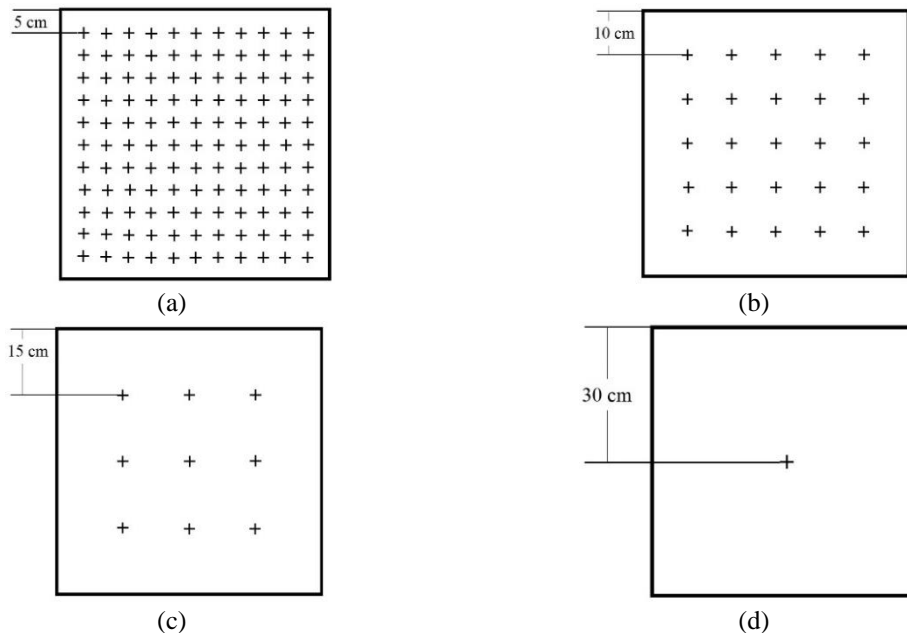


Fig. 11 Sketch of the four different stitching patterns: A (a), B (b), C (c), D (d)

constant value after a longer transient.

Furthermore, a comparison among the deflection amplitudes of the three TCs at each AoA for the untensioned and pre-tensioned cases has been made.

Since the LCOs were chaotic in time, the Root Mean Square (RMS) value of deflections amplitude was used. Fig. 10 shows the $w/h_{N(RMS)}$ amplitudes, as a function of dynamic pressure for all the TCs, for the untensioned and the pre-tensioned case. As expected, by increasing the number of layers, for equal values of the dynamic pressure, the deflection amplitude tends to decrease for both the untensioned and pre-tensioned cases. Moreover, at an AoA equal to 2.5° the TC 9 L is still stable, while the TCs 5 L and the 3 L are already in the LCO regime for the untensioned case.

Thus, as shown, when including the pre-tensioning in the solution, the TC 9 L is stable for all the flow conditions investigated, while the 5 L and the 3 L TC experience the LCO after 70 kPa.

Table 5 Natural frequencies

Frequency (Hz)	5 cm (A)	10 cm (B)	15 cm (C)	30 cm (D)
	Pre-tension 525 N/m	Pre-tension 525 N/m	Pre-tension 525 N/m	Pre-tension 525 N/m
f_{11}	48.85	48.84	48.82	48.12
f_{21}	84.71	84.68	84.34	79.16
f_{31}	135.61	135.58	134.93	137.75
f_{41}	202.18	202.17	200.25	200.25
f_{51}	285.32	285.30	285.7	285.76
f_{61}	385.52	394.29	387.15	394.29

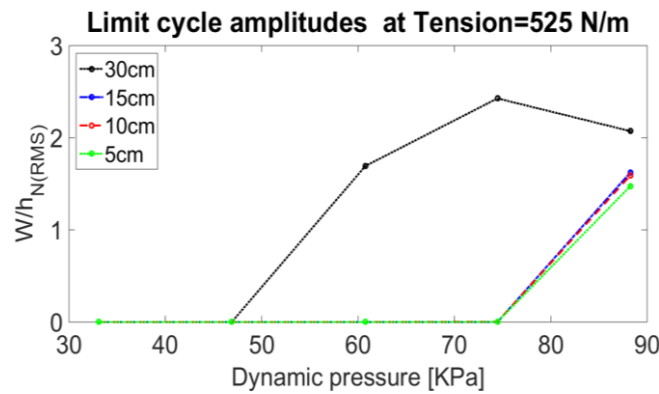


Fig. 12 Limit cycle amplitudes as a function of dynamic pressure: pre-tensioned

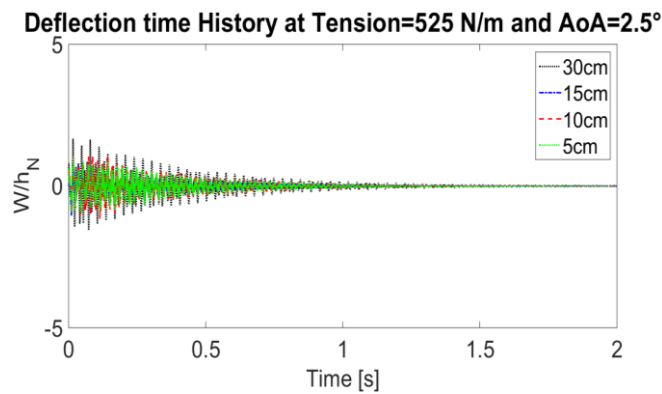


Fig. 13 Deflection time history comparison at $x/a, x/b=0.8,0.5$, $AoA=2.5^\circ$, pre-tensioned

5.2 The influence of the stitching density on the aero-elastic response

All the layers need to be perfectly bonded, in order to prevent hot gas from damaging the body of the entry capsule behind the TPS, but the weight of the stitch should be reduced in order to decrease the energy necessary for the launch. For those reasons, it is of interest to investigate the stitching density on the aero-elastic response of the TPS. Thus, in the present section the influence of the stitching density on the pre-tensioned 3 L case has been investigated.

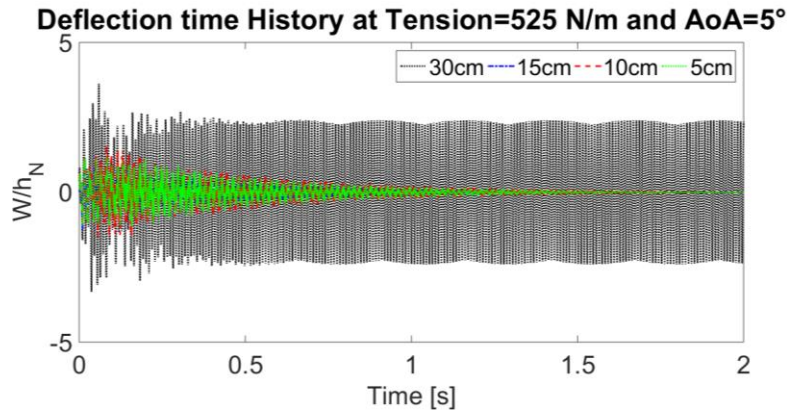


Fig. 14 Deflection time history comparison at x/a , $x/b=0.8,0.5$, $AoA=5^\circ$, pre-tensioned

Four TCs have been taken into account: The nominal case with the spacing between stitching point of 5 cm (TC A); a second case with a gap between stitching point of 10 cm (TC B); a third case with a spacing between stitching point of 15 cm (TC C); and a fourth case with a single stitching point in the middle of the TPS (TC D) (see Fig. 11).

Again, before calculating the aero-elastic response, the natural frequencies of the TPS using the eigenvalue extraction linear theory, neglecting the non-linear term S^{layer} , have been computed.

As was previously chosen for the validation of the 3L model, 6 half-waves in the flow direction and 1 half-wave in the spanwise direction, a value of the structural damping equal to 0.01, and a stitching stiffness k^{St} of 50000 Nm have been selected. Only the case with the pre-tension equal to 525 N/m has been studied for each TC. Natural frequencies for each TC have been summarized in Table 5.

Then, deflections time histories at the accelerometer location as a function of flow Mach number and dynamic pressure, as summarized in Table 2, were computed using the non-linear computational model outlined in Section 2. The simulation time has been set again to 8 seconds. Fig. 12 shows the w/h_N (RMS) amplitudes, as a function of dynamic pressure for all the TCs. As shown, while the TCs A, B, and C seem to show a similar, nearly stable, response up to the AoA equal to 7.5° , for the case D the LCO occurs at an angle of attack equal to 2.5° .

Figs. 13 and 14 show a comparison among the deflection time histories of the four different TCs, for the AoA equal to 2.5° and 5° , at 46 kPa and 60 kPa respectively. Since the transient is quite short, only the first 2 seconds have been depicted. As shown in Fig. 13, all the TCs exhibit a stable behavior. However, when the AoA is equal to 5° , as shown in Fig. 14, the deflections of the cases A, B and C tend to decrease with time, while the TC D presents a limit cycle behavior with a maximum RMS deflection w/h_N equal to 2.

6. Conclusions

The hypersonic, non-linear, aero-elastic behavior of a flexible, square, multi-layer TPS using a computational model based on the modes of the structure has been investigated.

The proposed model is in good agreement with the available theoretical and experimental results. Despite the simplifying assumptions, the code allows predicting the effect of the key

parameter trends in terms of peak frequencies and response amplitude.

The increase of the number of layers shifts the LCO phenomenon to higher dynamic pressures. Indeed, it has been shown that as the number of layers increases, the RMS of the w/h_N decreases.

An interesting result is the effect on the non-linear aero-elastic behavior of adding a pre-tension equal to 525 N/m to the TPS edges. The pre-tension stabilizes the vibrational behavior, and pushes forward the LCO phenomenon to values of the dynamic pressure higher than 60 kPa. Therefore, the computational model shows that, as expected, increasing the number of the layers or adding tension to the TPS decreases the nonlinear aero-elastic response.

Furthermore, there is small difference in terms of nonlinear aero-elastic response between TCs A, B and C. While the TC D experiences a LCOs at a dynamic pressure quite below the value of the cases A, B and C.

This result proves also that, if we ensure that all the 3 layers behave as a single panel up to 3 half-waves in the stream wise direction (i.e., TCs A,B and C), the appearance of the LCO phenomenon occurs at higher dynamic pressures. This is because the influence of the first few modes is much more critical as compared to the influence of the higher modes in the stream wise direction.

In conclusion, the relatively simple, but accurate, model presented, not only has demonstrated the feasibility of investigating the aero-elastic behavior of a flexible multi-layer TPS in hypersonic conditions; but its flexible formulation opens the way to several further studies such as the effect of different stitching shapes, the temperature field, and/or a more accurate aerodynamic theory like the third order PT or even a CFD aerodynamic model on the LCO behavior.

References

- Carandente, V. (2014), "Aerothermodynamic and mission analyses of deployable aerobraking earth re-entry systems", Ph.D. Dissertation.
- Carandente, V., Elia, G. and Savino, R. (2013), "Conceptual design of de-orbit and re-entry modules for standard cubesats", *Proceedings of the 2nd IAA Conference on University Satellite Missions and Cubesat Workshop*, Rome, February.
- Carandente, V. and Savino, R. (2014), "New concepts of deployable de-orbit and re-entry systems for cubesat miniaturized satellites", *Rec. Pat. Eng.*, **8**(1), 2-12.
- Carandente, V., Savino, R., D'Oriano, V. and Fortezza, R. (2014), "Deployable aerobraking earth entry systems for recoverable microgravity experiments", *Proceedings of the 65th International Astronautical Congress*, Toronto, Canada, September.
- Carandente, V., Savino, R., Iacovazzo, M. and Boffa, C. (2013), "Aerothermal analysis of a sample-return reentry capsule", *Flu. Dyn. Mater. Proc.*, **9**(4), 461-484.
- Carandente, V., Zuppari, G. and Savino, R. (2014), "Aerothermodynamic and stability analyses of a deployable re-entry capsule", *Acta Astronaut.*, **93**, 291-303.
- Dillman, R., DiNonno, J., Bodkin, R., Gsell, V., Miller, N., Olds, A. and Bruce, W. (2013), "Flight performance of the inflatable reentry vehicle experiment 3", *Proceedings of the 10th International Planetary Probe Workshop*, San Jose, U.S.A., June.
- Dillman, R., DiNonno, J., Bodkin, R., Gsell, V., Miller, N., Olds, A. and Bruce, W. (2010), "Flight performance of the inflatable reentry vehicle experiment II", *Proceedings of the International Planetary Probe Workshop*, Barcelona, Spain, June.
- Dowell, E. (1970), "Panel flutter: A review of aeroelastic stability of plates and shells", *AIAA J.*, **8**(3), 385-399.
- Dowell, E. (1975), *Aeroelasticity of Plates and Shells*, Springer, New York, U.S.A.

- Dugundji, J. (1966), "Theoretical considerations of panel flutter at high supersonic mach numbers", *AIAA J.*, **4**(7), 1257-1266.
- Ellen, C. (1965), "Approximate solution of the membrane flutter problem", *AIAA J.*, **3**(6), 1186-1187.
- Goldman, B. and Dowell, E. (2014), "Nonlinear oscillations of a fluttering plate resting on a unidirectional elastic foundation", *AIAA J.*, **52**(10), 2364-2368.
- Goldman, B., Dowell, E. and Scott, R. (2013), "Flutter analysis of the thermal protection layer on the NASA HIAD", *Proceedings of the 22nd AIAA Aerodynamic Decelerator Systems (ADS) Conference*, Florida, U.S.A.
- Goldman, B., Dowell, E. and Scott, R. (2014), "In-flight aeroelastic stability of the thermal protection system on the NASA HIAD, part I: Linear theory", *Proceedings of the 55th AIAA/ASME/ASCE/AHS/SC Structures, Structural Dynamics, and Materials Conference*, Maryland, U.S.A.
- Goldman, B., Dowell, E. and Scott, R. (2015), "In-flight aeroelastic stability of the thermal protection system on the NASA HIAD, part II: Nonlinear theory and extended aerodynamics", *Proceedings of the 56th AIAA/ASCE/AHS/ASC Structures, Structural Dynamics, and Materials Conference*, Florida, U.S.A.
- Goldman, B., Scott, R. and Dowell, E. (2014), *Nonlinear Aeroelastic Analysis of the HIAD TPS Coupon in the NASA 8' High Temperature Tunnel: Theory and Experiment*, NASA TM-2014-218267.
- Guruswamy, G. (2002), "A review of numerical fluids/structures interface methods for computations using high-fidelity equations", *Comput. Struct.*, **80**(1), 31-41.
- Hughes, S., Dillman, R., Starr, B., Stephan, R., Lindell, M., Player, C. and Cheatwood, F. (2005), "Inflatable re-entry vehicle experiment (IRVE) design overview", *Proceedings of the 18th AIAA Aerodynamic Decelerator Systems Technology Conference and Seminar*, Munich, Germany, May.
- Johns, D. (1971), "Supersonic membrane flutter", *AIAA J.*, **9**(5), 960-961.
- Kramer, R., Cirak, F. and Pantano, C. (2013), "Fluid-structure interaction simulations of a tension-cone inflatable aerodynamic decelerator", *AIAA J.*, **51**(7), 1640-1656.
- McNamara, J. and Friedmann, P. (2007), *Aeroelastic and Aerothermoelastic Analysis of Hypersonic Vehicles: Current Status and Future Trends*, Collection of Technical Papers-AIAA/ASME/ASCE/AHS/ASC Structures, Structural Dynamics and Materials Conference, 3814.
- McNamara, J. and Friedmann, P. (2011), "Aeroelastic and aerothermoelastic analysis in hypersonic flows: Past, present, and future", *AIAA J.*, **49**(6), 1089-1122.
- Mei, C., Abdel-Motagaly, K. and Chen, R. (1999), "Review of nonlinear panel flutter at supersonic and hypersonic speeds", *Appl. Mech. Rev.*, **52**(10), 321-332.
- Rohrschneider, R. (2007), "Variable-fidelity hypersonic aeroelastic analysis of thin-film ballutes for aerocapture", Ph.D. Dissertation, Georgia Institute of Technology, U.S.A.
- Savino, R. (2013), "Study and development of a sub-orbital reentry demonstrator", *Proceedings of the Italian Association of Aeronautics and Astronautics XXII Conference*, Naples, Italy, September.
- Savino, R. and Carandente, V. (2012), "Aerothermodynamic and feasibility study of a deployable aerobraking re-entry capsule", *Flu. Dyn. Mater. Process.*, **8**(4), 453-477.
- Scott, R., Bartels, R. and Kandil, O. (2007), "An aeroelastic analysis of a thin flexible membrane", *Proceedings of the 48th AIAA/ASME/ASCE/AHS/ASC Structures, Structural Dynamics, and Materials Conference*, Hawaii, U.S.A.
- Spriggs, J., Messiter, A. and Anderson, W. (1969), "Membrane flutter paradox-an explanation by singular perturbation methods", *AIAA J.*, **7**(9), 1704-1709.
- Wang, Z., Yang, S., Liu, D., Wang, X., Mignolet, M. and Bartels, R. (2010), *Nonlinear Aeroelastic Analysis for a Wrinkling Aeroshell/Ballute System*, Collection of Technical Papers-AIAA/ASME/ASCE/AHS/ASC Structures, Structural Dynamics and Materials Conference.
- Wilde, D. and Walther, S. (2001), "Inflatable re-entry and descent technology (IRDT)-further developments", *Proceedings of the 2nd International Symposium of Atmospheric Re-entry Vehicles and Systems*, Arcachon, France.

Nomenclature

a	Sample Length	N_x, N_y, N_{xy}	In-Plane Stress Resultants
b	Sample Width	N_x^A, N_y^A	Applied Tension in x and y Direction
D	Bending Stiffness	q	Dynamic Pressure $1/2 \rho v^2$
E	Young's Modulus	q_{nm}	Deflection Function Modal Coordinate
F	Airy stress Function	x_i, y_i	Stitch Location in x and y Direction
F_{app}	Magnitude Force	x_0, y_0	Force Location in x and y Direction
f_{nm}	Stress Function Modal Coordinate	δ	Dirac Function
h	Material Thickness	Δp	Pressure Loading on Panel
h_N	Nextel Thickness	ν	Poisson Ratio
k^{St}	Stitch's Spring Constant	w	Plate Deflection
m	Plate Mass Per Area		

Acronyms

AKK	Aluminized Kapton Kevlar	HTT	High Temperature Tunnel
AoA	Angle of Attack	IRVE	Inflatable Re-entry Vehicle Experiment
CATE	Computational Aero Thermo Elasticity	LCO	Limit Cycle Oscillation
FFT	Fast Fourier Transform	PT	Piston Theory
GVT	Ground Vibration Test	RMS	Root Mean Square
HDAD	Hypersonic Deployable Aerodynamic Decelerator	TC	Test Case
HIAD	Hypersonic Inflatable Aerodynamic Decelerator	TPS	Thermal Protection System